Progress In Electromagnetics Research C, Vol. 122, 215–228, 2022

Design of High-Selectivity Compact Quad-Band BPF Using Multi-Coupled Line and Short Stub-SIR Resonators

Halah I. Khani[1, *], Ahmed S. Ezzulddin[1], and Hussam Al-Saedi[2]

Abstract—This study presents a quad-band bandpass filter with high selectivity, compact size, and highly independent bands using a folded C-shape resonator, short stub-SIR resonator, and two folded L-shape resonators. The suggested structure consists of two separate filters. The upper filter is made up of a short stub-SIR resonator loaded on a C-shape resonator resonating at 2.59 GHz and 3.5 GHz, respectively. The lower filter is made up of two folded L-shape resonators resonating at 4.89 GHz and 6.15 GHz, respectively. The frequencies at which the filter resonates are designed and arranged with high independence. The proposed filter achieves insertion loss of −2.7 dB, −0.7 dB, 2.3 dB, and −0.4 dB, and return loss of −13.32 dB, −11.03 dB, −9.17 dB, and −17.89 dB, respectively. In addition, eight transmission zeros appeared. The proposed design has a compact size of $0.19\lambda g \times 0.15\lambda g$ and is built on an RO4350B substrate with a dielectric constant of 3.66, loss tangent of 0.0037, and thickness of 0.508 mm. Finally, the suggested filter is intended to be used in 5G mobile communications and international mobile telecommunications services.

1. INTRODUCTION

Fifth Generation (5G) mobile communication is progressively coming into view as the demand for high transmission rates grows. 5G can achieve higher channel capacity than fourth-generation networks (4G). The International Telecommunication Union-Radio Communication Sector (ITU-R, Geneva, Switzerland) proposed three common 5G usage scenarios in 2015 for 5G mobile communication: improved mobile broadband (eMBB), massive machine-type communications (mTC), and ultra-reliable and low-latency communication (uRLLC) [1]. High-integration, low-cost, and high-speed data transmission are demanded for these application scenarios. As a major element of wireless communication systems, multi-band bandpass filters (BPFs) with compact size, low loss, and wide passbands are envisioned as promising solutions to satisfy the requirements posed by 5G mobile communications [2–4]. The Federal Communications Commission (FCC) and the Confederation of European Posts and Telecommunications (CEPT) have recently launched investigations into the feasibility of deploying International Mobile Telecommunications (IMT) services in the 5.9–7.1 GHz band (specifically, US 5.9–7.1 GHz and EU 5.9–6.4 GHz), with the possibility of making all or part of this band available for unlicensed operation [5]. This situation indicates that 5G sub-6 GHz will soon evolve into 5G sub-7 GHz. The 3.5 GHz spectrum is appealing for 5G since it is virtually universally available and can provide up to 100 MHz of bandwidth per operator [6].

A microstrip bandpass filter (BPF) is important in the RF front ends. With the growth of multi-service wireless communication networks, quad-band BPF with high performance has received a lot of attention, and many design strategies have been documented. Combining many resonators with shared input and output ports to generate a quad-band BPF is the most direct method, but it has a

Received 29 May 2022, Accepted 3 August 2022, Scheduled 12 August 2022
* Corresponding author: Halah I. Khani (eee.19.22@grad.uotechnology.edu.iq).
[1] Department of Electrical Engineering, University of Technology-Iraq, Bagdad, Iraq. [2] Department of Communications Engineering, University of Technology-Iraq, Bagdad, Iraq.

somewhat large circuit size [7]. In [8], by cascading two dual-band BPFs together with a single metallic via-holed feed line, a quadruple-band BPF was achieved. In [9], a short-end stub-loaded resonator provides the third passband, while the other multi-stub-loaded resonators operate at the first, second, and fourth passbands. In [10], quad-band BPF is achieved by using two stub-loaded nested dual-band loop resonators. Two sets of short stub-loaded E-shaped resonators are used to create a quad-band BPF in [11]. The second method is to use a double-layered structure to minimize the total circuit size of the quad-band BPF, but this increases fabrication complexity [12]. The third design method uses a single basic resonator to achieve a filter with a small size. [13] proposes a quad-band BPF based on a new stub-loaded stepped impedance resonator. Nonetheless, the bandwidths of the proposed design cannot be controlled independently. Because each passband has one transmission zero (TZ) on both sides, the lower and higher stopbands do not suppress well at the same time.

This article presents the design and implementation of microstrip compact quad-band BPF with a full systematic procedure. The employed resonators are a short stub-SIR resonator for 2.59 GHz, a folded C-shape resonator for 3.5 GHz, and two folded L-shape resonators for 4.89 GHz and 6.15 GHz intended to use for 5G mobile communications and international mobile telecommunications services (IMT). Because of the strong coupling between the resonators and feedlines, many Transmission Zeros (TZs) are generated, which could increase the performance of the given filter. In addition, adding interdigital capacitance to the proposed feedline increased the number of TZs. The proposed filter is built on an RO4350B substrate with a dielectric constant of 3.66, loss tangent of 0.0037, and thickness of 0.508 mm.

2. THE SUGGESTED QUAD-BAND BPF DESIGN

2.1. Specifications of the Suggested Filter

Based on the limitations placed by a set of 5G requirements, Table 1 lists the proposed compact quad-band BPF specifications.

Table 1. Specifications of the suggested filter.

Band	Center frequency f_o (GHz)	$\Delta f\%$	Order (N)	Application
1	2.59	7%	2	Mobile communication
2	3.5	5.7%	2	
3	4.89	3%	2	
4	6.15	8.1%	4	IMT Services

2.2. Theoretical Performance of the Proposed Filter

The filter requirements are translated into the M_{ij}, R_1, and R_2 elements of the appropriate coupling matrix. The goal is to convert these coupling components into physical dimensions. The suggested filter will be analyzed using the super-position technique. The g_k values corresponding to a return loss of 20 dB, and the elements of the coupling matrix are determined by using the formula from [14]. Table 2

Table 2. Calculation g values and coupling matrix for the proposed filter.

Band	g_0	g_1	g_2	g_3	Coupling matrix	$R_1 = R_2$
1 2 3 4	1	0.6667	0.5455	1.2222	$\begin{bmatrix} 0 & 1.6583 \\ 1.6583 & 0 \end{bmatrix}$	1.5

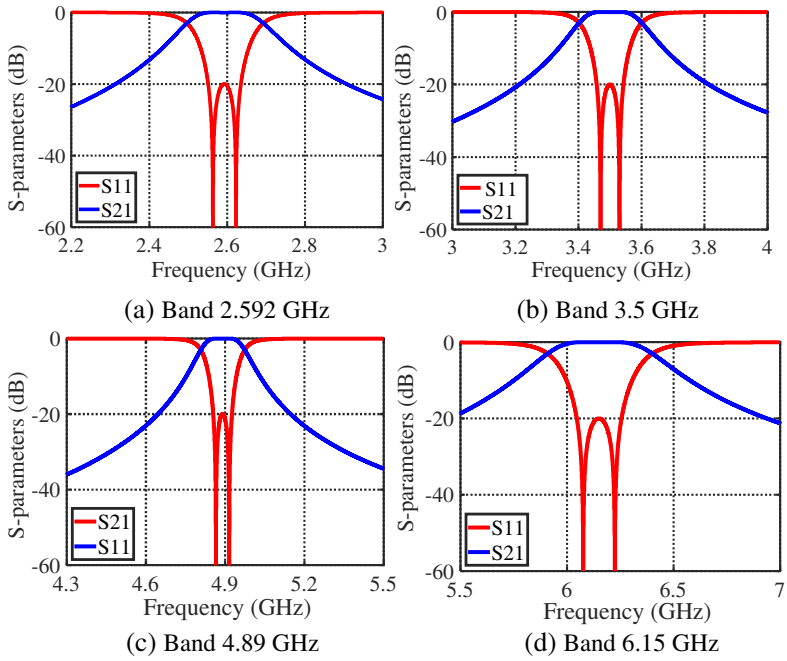

Figure 1. The simulated theoretical response of the filter based on the coupling matrix model.

summarizes the results. The filter S-parameters are given by equations in [14]. Figure 1 displays the simulated theoretical responses of the proposed filter employing the coupling matrix elements of the two-pole filter for band1, band2, band3, and band4 using the Superposition approach.

2.3. The Proposed Resonators

The presented structure consists of two parts that are used to match the impedance to 50 Ω. As shown in Figure 2(a), the upper part consists of a C-shape resonator loaded by a short stub-SIR resonator. Firstly, the C-shape resonator dimensions were adjusted using eigenmode analysis until the resonance frequency was reached, and then the l_2 of the C-shape resonator was miniaturized by 65.1% of its original length using the folded line technique, as illustrated in Figure 2(b). This resonator would produce 3.5 GHz. Secondly, by adding a short stub-SIR resonator to the C-Shape resonator as shown in Figure 3 to produce a band at 2.592 GHz, the upper part would convert from a single-mode resonator and create a single-band to the dual-mode resonator, creating dual-bands, and with the presence of the via-hole in the loaded stub-SIR resonator, which can be considered a miniaturized resonator. To investigate the dual-mode resonator when mode-1 is varied, mode-2 remains constant or almost constant and vice versa, as shown in Figure 4(a) and Figure 4(b).

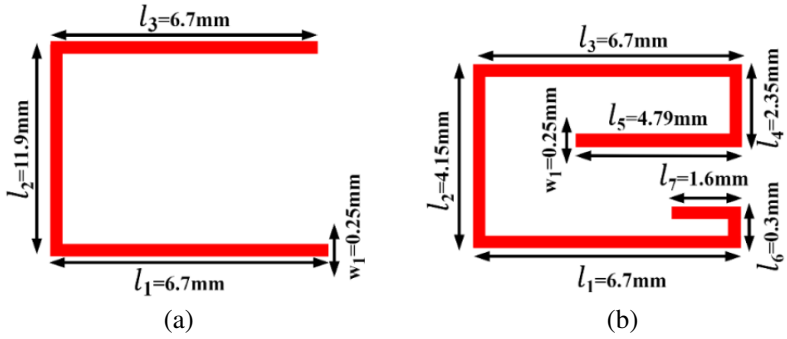

Figure 2. (a) C-shape resonator. (b) Miniaturization of a C-Shape using a folding line technique.

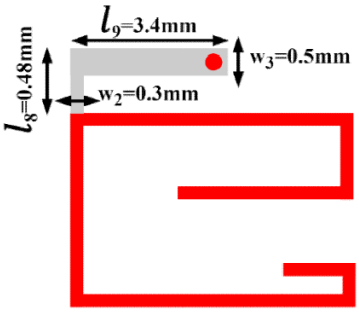

Figure 3. The configuration of the proposed dual-mode resonator.

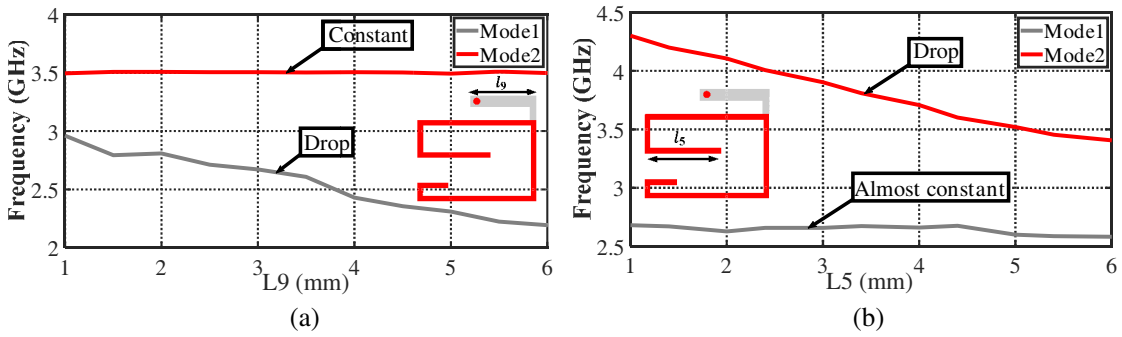

Figure 4. Eigen Modal solver setup of miniaturize dual mode. (a) The variation of the first mode. (b) The variation of the second mode.

Figure 5. The configurations of the suggested resonators. (a) L-shape resonator for 6.15 GHz, and (b) L-shape resonator for 4.89 GHz.

As shown in Figure 5, the lower part consists of two single-mode L-shape resonators, and these resonators will produce two bands, 4.89 GHz and 6.15 GHz. The eigenmode analysis method was used to analyze the two L-shape resonators. The dimensions of the L-shape resonators were tuned until the resonance frequency was reached. For the first L-shape resonator that produced 6.15 GHz, L_{11} was miniaturized by 53%, and for the second L-shape resonator that produce 4.89 GHz, L_{14} was miniaturized by 76% from their original lengths by using the folded line technique as shown in Figure 6.

2.3.1. Calculation of Interresonator Coupling

By using eigenmode analysis with the use of electrical and magnetic symmetry, the required gap that meets the coupling value M_{ij} can be calculated by using Equation (1). By applying a parametric sweep for the gap and inserting the relation between the coupling factors with the electric resonance f_e and

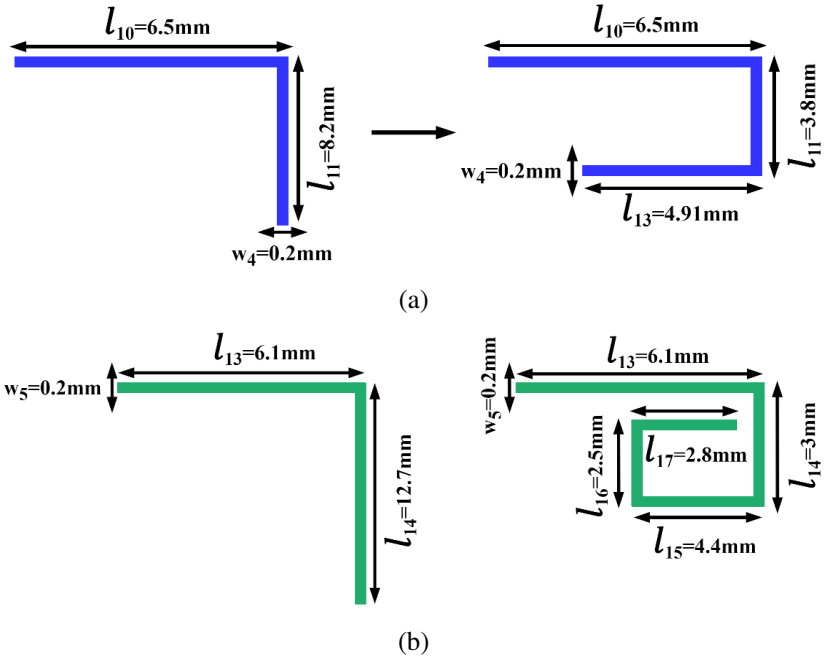

Figure 6. (a) Miniaturization of L-Shape for 6.15 GHz using a folding line technique, and (b) miniaturization of L-Shape for 4.89 GHz using a folding line technique.

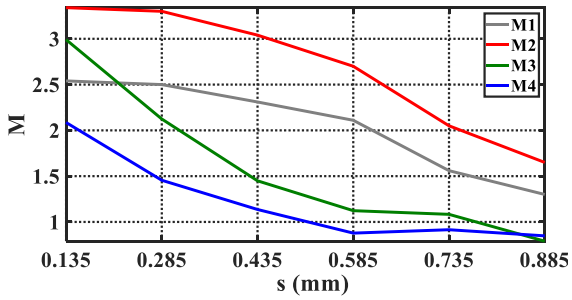

Figure 7. Coupling factor vs g.

magnetic resonance f_m, the coupling factor of the quad-band is determined as illustrated in Figure 7.

$$M = \frac{f_0}{BW}\frac{f_m^2 - f_e^2}{f_m^2 + f_e^2} \tag{1}$$

2.3.2. Calculation of Input/Output Coupling Using Group Delay Method

Input and output coupling can be synthesized by using the group delay matching method to realize the required input and output coupling based on Equations (2) and (3). The group delays at resonance for the four bands are 2.1 ns, 2.1 ns, 2.24 ns, and 0.85 ns.

$$\tau = \frac{4Q_e}{\Omega_0}\frac{1}{1 + \left(2Q_e\left(\Omega - \Omega_0\right)/\Omega_0\right)^2} \tag{2}$$

$$R = \frac{4}{\left(\Omega_2 - \Omega_1\right)}\frac{1}{\tau\left(\Omega_0\right)} \tag{3}$$

The proposed resonators and other components are shown in Figure 8. The values of microstrip transmission lines and resonator gaps (all in millimeters) are shown in Table 3.

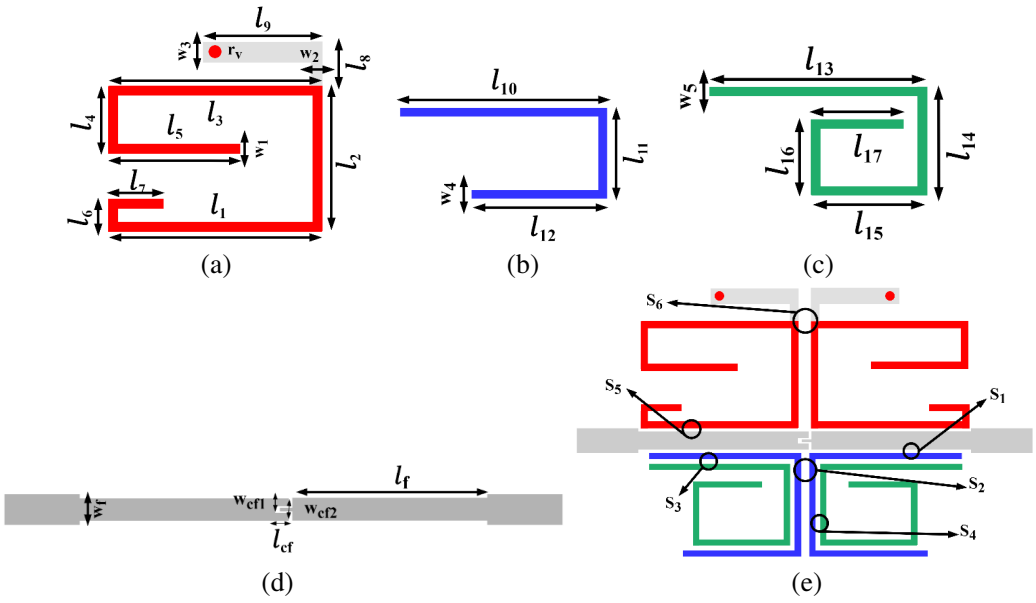

Figure 8. The suggested design parts (a) dual-mode resonator, (b) folding L-Shape for 6.15 GHz, (c) folding L-Shape for 4.89 GHz, (d) feedline, and (e) gaps for the final configuration.

Table 3. Dimensions of the quad-band BPF.

Parameter	w_p	l_P	l_f	w_f	l_{cf}	w_{cf1}	w_{cf2}	l_1	l_2
Dimension (mm)	1	3	6.8	0.75	0.3	0.24	0.1	6.7	4.15
Parameter	l_3	l_4	l_5	l_6	l_7	l_8	l_9	w_1	s_1
Dimension (mm)	6.7	2.35	5.2	0.3	1.6	0.45	3.35	0.25	0.125
Parameter	s_2	w_2	w_3	r_v	l_{10}	l_{11}	l_{12}	w_4	s_3
Dimension (mm)	0.4	0.3	0.5	0.15	6.5	3.8	5.35	0.2	0.125
Parameter	s_4	l_{13}	l_{14}	l_{15}	l_{16}	l_{17}	w_5	s_5	s_6
Dimension (mm)	0.35	6.1	3	4.4	2.3	2.89	0.2	0.2	0.2

2.4. Analysis of the Proposed Filter

In this section, the proposed filter will be analyzed by using the superposition technique. ANSYSEDT full-wave simulator was used to run all simulations. In Figure 9, the simulation results are presented for the C-shape resonator. This resonator creates a resonance frequency of 3.45 GHz. The bandwidth occurs between 3.33 GHz and 3.58 GHz with Δf of 7.2%. The passband poles are located at 3.41 GHz and 3.5 GHz with S_{11} values of -23.77 dB and -19.33 dB, respectively. The value of S_{21} is -0.6 dB. In addition, two transmission zeros appeared at 2.72 GHz and 4.03 GHz with S_{21} values of -69.84 dB and -49.03 dB, respectively.

In Figure 10, frequency responses (S_{11} and S_{21} parameters) of the upper dual-mode, which consists of a folded C-shape resonator and is loaded with a short stub-SIR resonator and suggested feedline, are plotted. According to the result shown in the figure that was mentioned above, two resonance frequencies are created, with the first resonance frequency around 2.56 GHz. The bandwidth ranges from 2.51 GHz to 2.62 GHz, with Δf of 4.29%. The passband pole is located at 2.56 GHz with an S_{11} value of 33.46 GHz, and the value of S_{21} is -0.5 dB. In addition, two transmission zeros appeared at 1.85 GHz and 2.79 GHz with S_{21} values of 72.99 dB and 50.53 dB, respectively. The second resonance frequency is created at 3.48 GHz. The bandwidth occurs between 3.39 GHz and 3.59 GHz with Δf

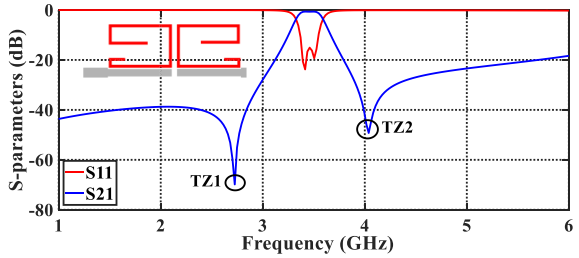

Figure 9. Feedline and C-shape structures frequency responses.

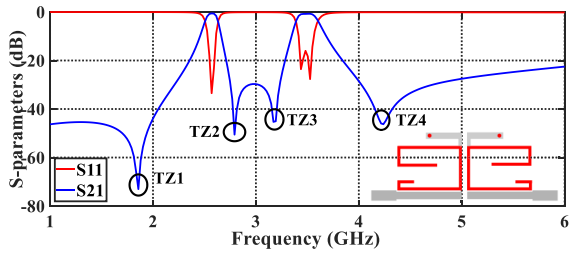

Figure 10. Feedline and dual-modes structures frequency responses.

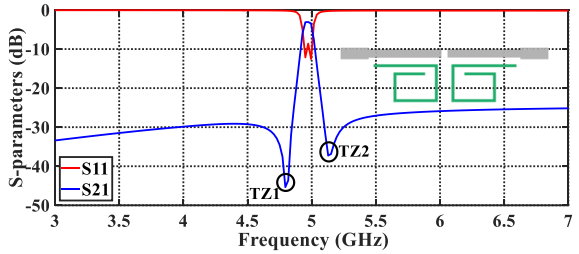

Figure 11. Frequency responses of feedline and folded L-shape of 4.89 GHz structures.

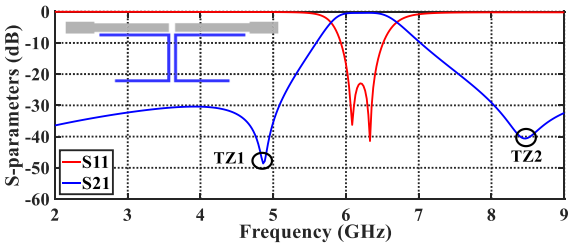

Figure 12. Frequency responses of feedline and folded L-shape of 6.15 GHz structures.

of 5.75%. The passband poles are located at 3.43 GHz and 3.5 GHz with S_{11} values of 23.55 dB and 27.65 dB, respectively, and the value of S_{21} is -0.7 dB. In addition, two transmission zeros appeared at 3.19 GHz and 4.23 GHz with S_{21} values of 45.03 dB and 46.25 dB, respectively.

In Figure 11, the simulation results are presented for the folded L-shape resonator structure that created the third band. This structure creates a resonance frequency of 4.97 GHz. The poles of the third band are 4.95 GHz and 4.99 GHz with S_{11} values of -12.12 dB and -12.52 dB, respectively. The value of S_{21} is -3 dB. In addition, two transmission zeros are created, which are located at 4.79 GHz and 5.12 GHz with S_{21} values of 45.33 dB and 37.25 dB, respectively.

Figure 12 illustrates the frequency responses (S_{11} and S_{21} parameters) of the folded L-shape resonator that formed the fourth band and suggested feedline. According to the figure mentioned above, the resonance frequency is created at 6.21 GHz. The bandwidth occurs between 5.8 GHz and 6.67 GHz, with Δf of 14%. The band resonance poles are located at 6.08 GHz and 6.33 GHz with S_{11} values of 36.23 dB and -41.4 dB, respectively, and the value of S_{21} is -0.4 dB. Moreover, two transmission zeros appear at 4.86 GHz and 8.46 GHz with S_{21} values of 48.59 dB and 40.62 dB, respectively

Finally, all existing resonators are used to analyze the complete structure of the proposed filter, as shown in Figure 13(a). Figure 13(b) shows the simulations of S-parameters. According to the result shown in the figure mentioned above, the resonance frequency of the first band is located at 2.59 GHz, which is formed by the loaded short stub-SIR resonator. The bandwidth occurs between 2.54 GHz and 2.64 GHz with Δf of 3.84%. The poles of the resonant band are located at 2.569 GHz and 2.614 GHz with S_{11} values of 20.84 dB and -21.66 dB, respectively, and the value of S_{21} is -1 dB. Furthermore, at 1.96 GHz and 2.79 GHz, two transmission zeros appear with S_{21} values of 79.72 dB and 50.9 dB, respectively. The second band resonance frequency is located at 3.5 GHz, which is formed by the folded C-shape resonator. The bandwidth occurs between 3.4 and 3.6 GHz, with an f of 5.75%. The band poles are located at 3.45 GHz and 3.52 GHz with S_{11} values of 21.03 dB and -22.25 dB, respectively. The value of S_{21} is -0.7 dB. At 3.17 GHz, only one transmission zero was formed at S_{21} values of 54.57 dB. For the third band, the resonance frequency is 4.89 GHz, which is created by the second lower folded L-shape resonator. With Δf of 3.4%, the bandwidth is between 4.78 GHz and 4.95 GHz. The band poles are located at 4.83 GHz and 4.92 GHz with S_{11} values of 22.1 dB and -18.5 dB, respectively, and the value of S_{21} is -1.3 dB. However, just one transmission zero is created at 5.08 GHz with an

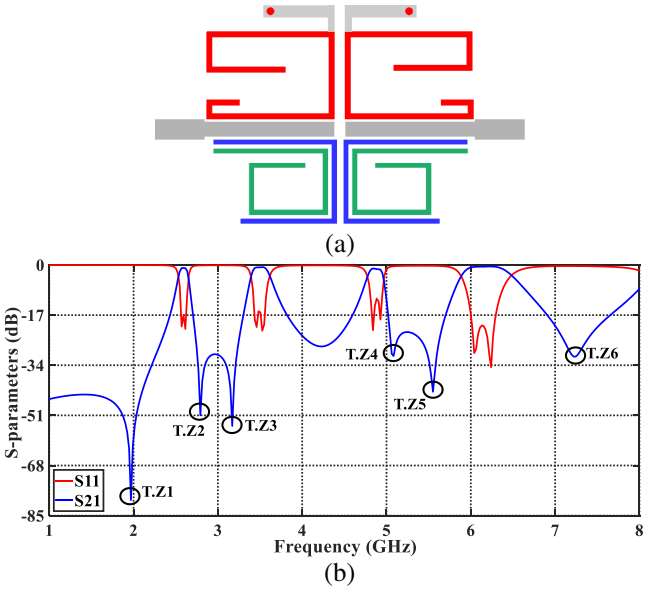

Figure 13. (a) Quad-band BPF structure, and (b) frequency responses of Quad-band BPF structure.

S_{21} value of 30.83 dB. The fourth resonance frequency is located at 6.15 GHz to form the fourth band, which is created by the first lower folded L-shape resonator. The bandwidth occurs between 5.9 GHz and 6.4 GHz with Δf of 8.1%. The band poles are located at 6.04 GHz and 6.24 GHz with S_{11} values of 29.84 dB and 34.66 dB, respectively, and the value of S_{21} is 0.5 dB. In addition, two transmission zeros appear located at 5.55 GHz and 7.24 GHz with S_{21} values of 42.97 dB and 31.08 dB, respectively.

Interdigit capacitance will be added to the suggested feedline as shown in Figure 14(a) to add more TZs to the proposed structure, resulting in a high-selectivity response. Figure 14(b) depicts the

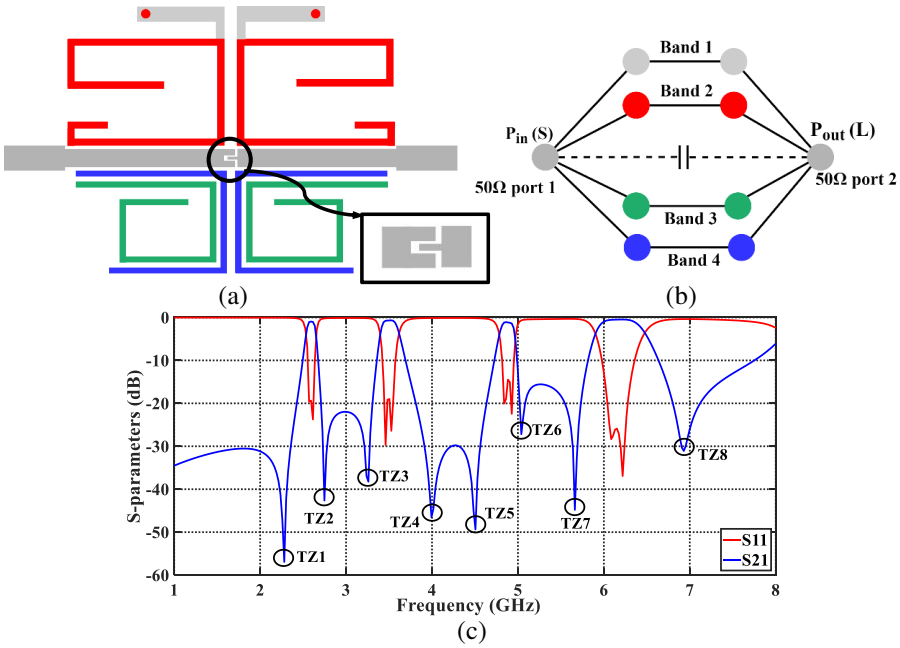

Figure 14. (a) Quad-band BPF structure, (b) coupling scheme and (c) frequency responses of Quad-band BPF structure.

simulated S-parameters of the proposed high-selectivity and very compact quad-band BPF. According to Figure 14(b), the loaded short stub-SIR resonator generates the first resonance frequency around 2.59 GHz. The bandwidth occurs between 2.54 GHz and 2.64 GHz with Δf of 3.84%. The passband poles are located at 2.569 GHz and 2.614 GHz with S_{11} values of 19.583 dB and −23.741 dB, respectively, and the value of S_{21} is −0.9 dB. Furthermore, two transmission zeros are created at 2.28 GHz and 2.74 GHz with S_{21} values of 56.91 dB and 42.61 dB, respectively. The second resonance frequency is around 3.5 GHz, which is created by the folded C-shape resonator. The bandwidth is between 3.4 GHz and 3.6 GHz, with Δf of 5.75%. The poles of the resonant band are at 3.45 GHz and 3.52 GHz with S_{11} values of 29.7 dB and 26.38 dB, respectively, and the value of S_{21} is 0.6 dB. Additionally, the transmission zero resonant bands are created at 3.25 GHz and 3.99 GHz with S_{21} values of −38.22 dB and −46.5 dB, respectively. The third resonance frequency is created at 4.89 GHz, which is formed by the second folded L-shape resonator. With Δf of 3.4%, the bandwidth is between 4.8 GHz and 4.97 GHz. The resonance poles of the band are 4.83 GHz and 4.92 GHz with S_{11} values of −20.04 dB and −22.43 dB, respectively, and the value of S_{21} is −1.1 dB. Moreover, two transmission zeros of the resonant band are created at 4.5 GHz and 5.03 GHz with S_{21} values of −49.34 dB and −27.17 dB, respectively. The fourth band is formed by the first lower folded L-shape resonator, which creates a resonance frequency of 6.15 GHz. The bandwidth occurs between 5.9 GHz and 6.4 GHz with Δf of 8.1%. The poles of the resonant band are located at 6.08 GHz and 6.21 GHz with S_{11} values of −28.33 dB and −36.9 dB, respectively, and the value of S_{21} is −0.4 dB. In addition, two transmission zeros appeared at 5.66 GHz and 6.93 GHz with S_{21} values of −44.79 dB and −31.07 dB, respectively. As a result, the total number of transmission zeros becomes eight after adding the interdigit capacitance. Furthermore, the interdigit capacitance enhances the return loss. Figure 15 shows the comparison of the results with and without interdigit capacitance. The dimensions of the proposed quad-band BPF shown in Figure 14(a) are 14 mm × 10.8 mm ($0.19\lambda g \times 0.15\lambda g$) where λg is the guided wavelength at 2.592 GHz, and size is 151.2 mm^2 ($0.0285\lambda g^2$).

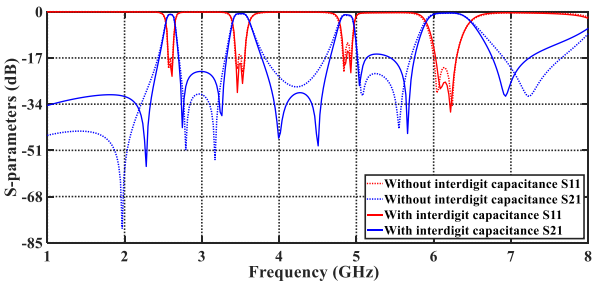

Figure 15. Quad-band BPF frequency responses comparison with and without interdigit capacitance.

The property of independence will be studied according to the theory shown in Figure 16. The first passband F_{b1} can be adjusted by changing the dimensions of the short stub-SIR resonator, and the second passband F_{b2} can be adjusted by changing the dimensions of the C-shape resonator. The third passband F_{b3} can be adjusted by changing the dimensions of the second L-shape resonator. Finally, the fourth passband Fb4 can be adjusted by changing the dimensions of the first L-shape resonator.

Figure 17(a) and Figure 17(b) illustrate the parametric simulation results for the $|S_{11}|$ and $|S_{21}|$ characteristics following the changing of l_9, respectively. It is seen from Figure 17(a) that the frequency of F_{b1} can be adjusted by varying l_9; when $l_9$increases by 59.7%, the frequency of F_{b1} will shift independently to the lower frequencies, and when l_9 decreases by 59.7%, the frequency of F_{b1} will shift independently to the higher frequencies. $F_{b2,}$ $F_{b3,}$ and F_{b4} will be stable. It is also shown that the values of $|S_{11}|$ and $|S_{21}|$ are better than −8 dB and −3 dB, respectively, and l_9 can control the passband F_{b1}.

The magnitudes of $|S_{11}|$ and $|S_{21}|$ characteristics following the change in l_5 are displayed in Figure 18(a) and Figure 18(b), respectively. It is noted from Figure 18(b) that F_{b2} shifts independently to the lower frequencies when l_5 increases by 20%, and when l_5 decreases by 57.6%, F_{b2} will shift independently to the higher frequency F_{b3}, and F_{b4} remains constant without any effect while having a little effect on the F_{b1} at the same time. The value $|S_{11}|$ is better than −15 dB and −3 dB, respectively,

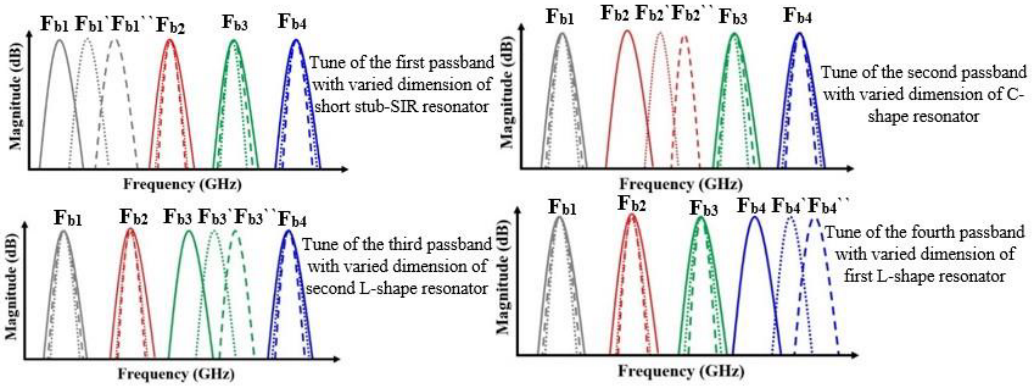

Figure 16. The independent filter response with varied resonator dimensions.

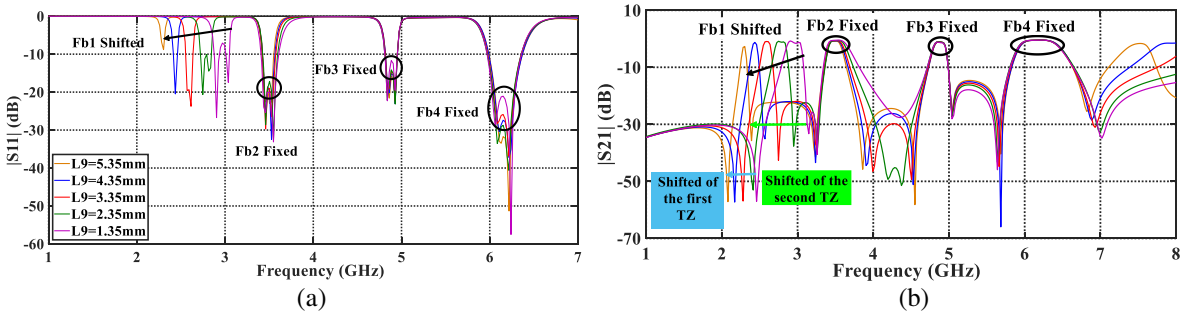

Figure 17. (a) Simulation results for $|S_{11}|$ with multiple l_9 values and (b) simulation results for $|S_{21}|$ with multiple l_9 values.

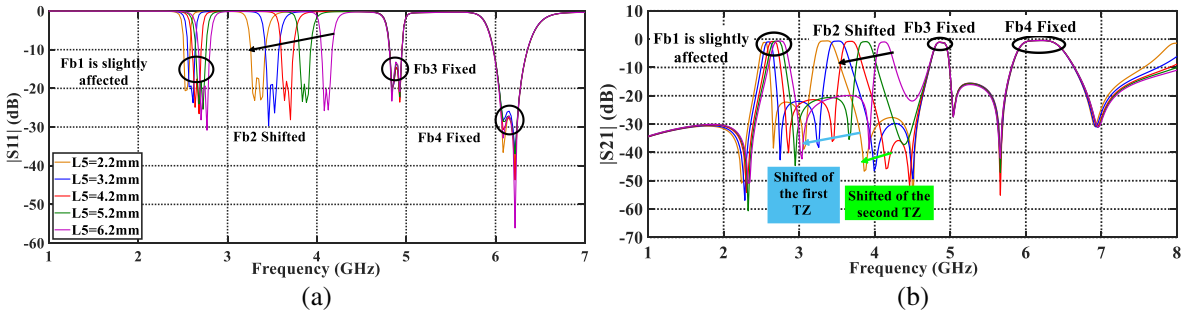

Figure 18. (a) Simulation results for $|S_{11}|$ with multiple l_5 values and (b) simulation results for $|S_{21}|$ with multiple l_5 values.

indicating that the quad-band BPF has a low reflection coefficient, and l_5 can control the passband F_{b2}. Figure 19(a) and Figure 19(b) illustrate the parametric simulation results for the $|S_{11}|$ and $|S_{21}|$ characteristics following the changing of l_{13}, respectively. It is seen from Figure 19(a) that the frequency of F_{b3} can be adjusted by varying l_{13}; when L_{13} increases by 33%, the frequency of F_{b3} will shift independently to the lower frequencies, and when l_{13} decreases by 33%, the frequency of F_{b3} will shift independently to the higher frequencies. F_{b1}, F_{b2}, and F_{b4} will remain stable without any effect while having a little effect on the F_{b4}. It is also shown that the values of $|S_{11}|$ and $|S_{21}|$ are better than -15 dB and -3 dB, respectively, and l_{13} can control the passband F_{b3}. The magnitude of the $|S_{11}|$ and $|S_{21}|$ characteristics following the change in l_{12} are displayed in Figure 20(a) and Figure 20(b), respectively. It is noted from Figure 20(b) that F_{b4} shifts independently to the lower frequencies when l_{12} increases by 38%. When l_{12} decreases by 38%, F_{b4} will shift independently to the higher frequencies F_{b1}, and

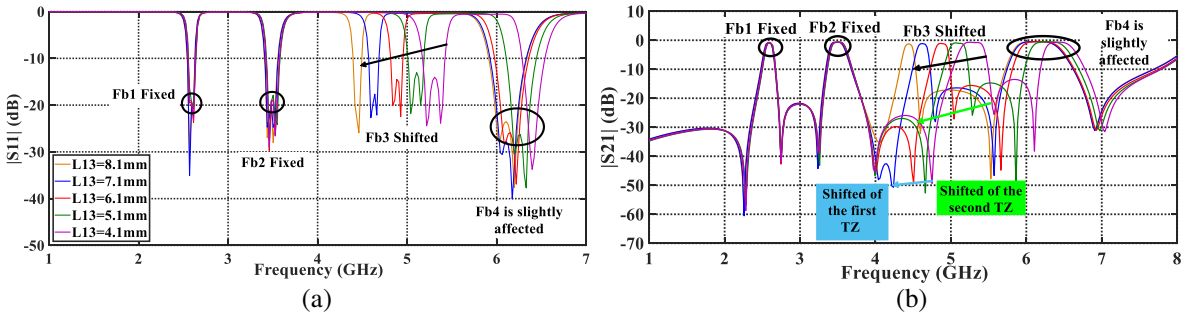

Figure 19. (a) Simulation results for $|S_{11}|$ with multiple l_{13} values and (b) simulation results for $|S_{21}|$ with multiple l_{13} values.

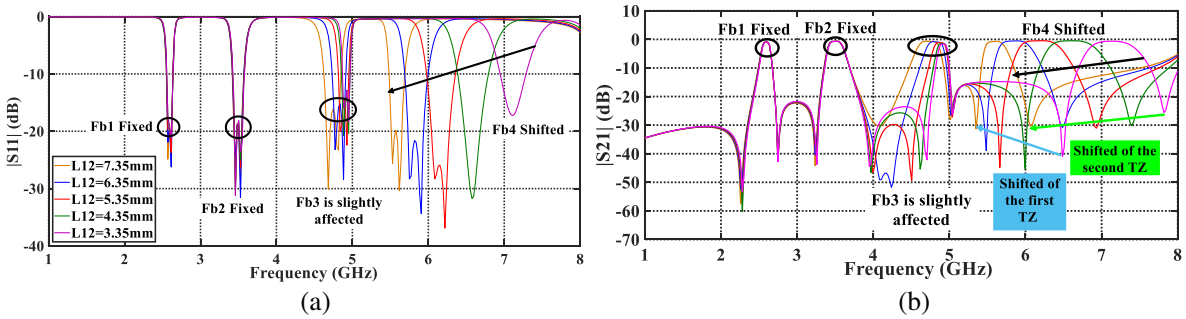

Figure 20. (a) Simulation results for $|S_{11}|$ with multiple l_{12} values and (b) simulation results for $|S_{21}|$ with multiple l_{12} values.

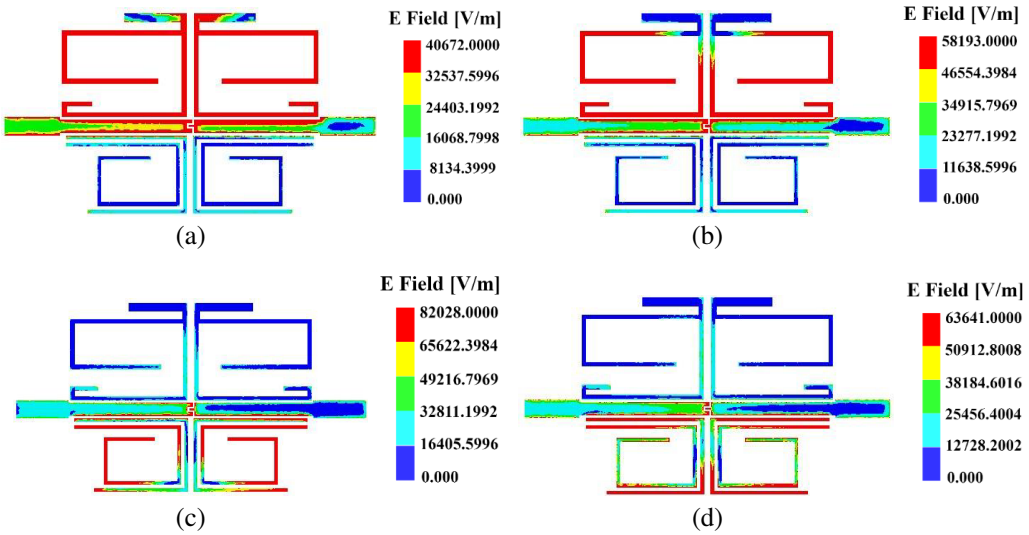

Figure 21. Surface current flow at (a) F_{b1} and F_{b2}, (b) F_{b2}, (c) F_{b3} and (d) F_{b4}.

F_{b2} remains constant without any effect while having a little effect on the F_{b3} the same time. The value $|S_{11}|$ is better than -15 dB and -3 dB, respectively, indicating that the quad-band BPF has a low reflection coefficient, and l_{12} can control the passband F_{b4}. These results indicate that the four passband frequencies can be adjusted individually, proving the design of a highly independent quad-band BPF.

Surface current flows at F_{b1}, F_{b2}, F_{b3}, and F_{b4} are depicted in Figures 21(a), 21(b), 21(c), and 21(d), respectively. The current passed through the upper portion of the F_{b1}, F_{b2} passbands. The F_{b2}

band surface current has flowed via the C-shaped structure. At the lowest half of the feeding structure, the currents at F_{b3} and F_{b4} passbands have flowed. This shows that the resonator operates highly independently.

2.5. Measurement Result

A sample of the compact quad-band BPF with the dimensions listed in Table 3 has been fabricated and measured. The top view photograph of the measured sample is shown in Figure 22. To validate the recommended design flow, the compact quad-band BPF is built on an RO4350B substrate with a dielectric constant of 3.66, loss tangent of 0.0037, and thickness of 0.508 mm. The manufactured filter is measured using a VNA (vector network analyzer).

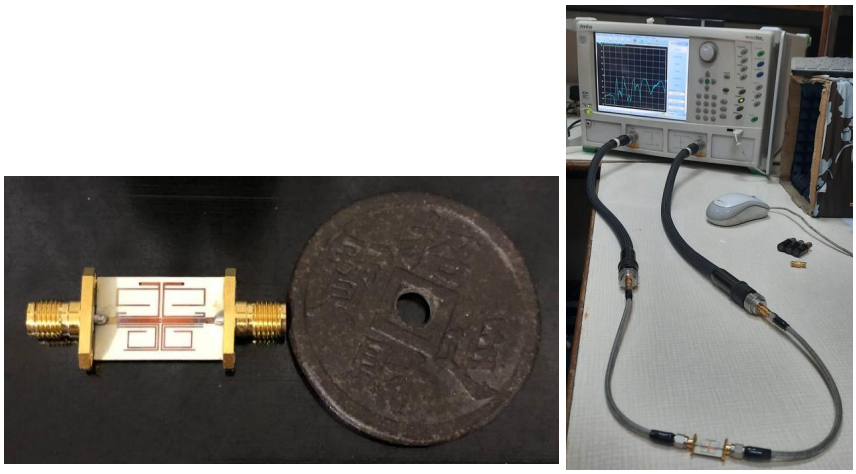

Figure 22. Measurement Photograph of the fabricated filter.

Figure 23 depicts the comparison between simulated and measured results. According to these results, the four passbands measured are centered at 2.62 GHz, 3.5 GHz, 4.9 GHz, and 6.22 GHz. The minimum insertion losses for each band are −2.7 dB, −0.7 dB, −2.3 dB, and −0.4 dB, and the return losses are −13.32 dB, −11.03 dB, −9.17 dB, and −17.89 dB, respectively, and eight TZs located at 2.26 GHz, 2.8 GHz, 3.24 GHz, 4.08 GHz, 4.44 GHz, 5.06 GHz, 5.7 GHz, and 7.02 GHz with S_{21} values of −54.13 dB, −21.26 dB, −30.28 dB, and −26.39 dB. Figure 23 likewise indicates that the simulated and measured results are very close. The few little differences between the results are related to substrate parameter tolerances. The little shift in the frequency is related to ε_r tolerances, whereas the tolerance in the loss tangent causes attenuation. Furthermore, the fabrication tolerance of the filter structure will introduce extra inaccuracies in the position of the resonant bands. Another factor that influences the measurement is the non-ideal SMA/transition. This will result in increased attenuation and undesired

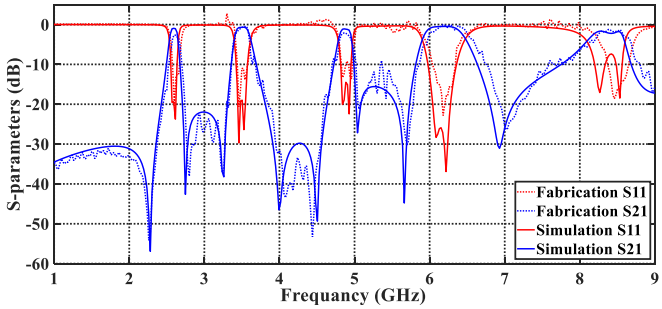

Figure 23. Simulated and measured results comparison of the proposed quad-band BPF.

Table 4. Performance comparison of this work with other filters.

Ref.	Passband (GHz)	$\|S_{21}\|$ (dB)	$\|S_{11}\|$ (dB)	Size λg^2	TZ	Independent passband (b1/b2/b3/b4)
[15]	2.4/3.5/ 5.2/5.8	1.8/1.5/ 2.1/2.9	18/30/ 28.7/27.6	0.0529	7	yes/yes/ no/no
[16]	1.5/3.6/ 5.4/7.25	0.2/0.6/ 1.8/1.7	25.9/27.8/ 14.8/12.2	0.021	4	yes/yes/ yes/yes
[17]	1.57/2.4 3.5/5.2	5.18/2.79/ 2.82/5.19	> 15	0.0512	7	yes/yes/ yes/yes
[18]	1.45/1.65/4/6	1.05/1.04/ 0.8/2.8	> 18	0.13	6	yes/yes/ yes/yes
[19]	2/2.7/ 3.45/4.6	1.6/1.6/ 1.3/1.5	> 10	0.0504	5	yes/no yes/no
[20]	1.51/2.83/ 4.70/5.75	0.44/0.96/ 1.35/1.66	> 12	0.0625	7	NA
[21]	2.25/2.76/ 4.6/7.45	1.05/1.04/ 0.8/2.8	19.5/11.8/ 20.8/14.8	0.0456	2	NA
This work	2.62/3.5 4.9/6.22	2.7/0.7/ 2.3/0.4	13.32/11.03/ 9.17/17.89	0.0285	8	yes/yes /yes/yes

situations of measurement devices like calibration, which was the cause of the ripple. Comparisons between this work and other filters are made in Table 4.

3. CONCLUSIONS

The design and implementation of a full systematic procedure and a high-selectivity, compact, and highly independent quad-band BPF are described in this work. The presented structure consists of two separate filters; the upper filter comprises a short stub-SIR resonator loaded on a C-shape resonator resonating at 2.62 GHz and 3.5 GHz, respectively. The lower filter comprises two folded L-shape resonators resonating at 44.9 GHz and 6.22 GHz, respectively. The frequencies at which the filter resonates are designed and arranged with high independence. A folding structure and a via-hole were proposed to miniaturize the quad-band BPF resonators. The proposed filter achieves insertion loss of -2.7 dB, -0.7 dB, 2.3 dB, and -0.4 dB, and return loss of -13.32 dB, -11.03 dB, -9.17 dB, and -17.89 dB, respectively. In addition, eight transmission zeros appeared. The proposed filter intended for the use in 5G mobile communication and IMT services. The proposed filter has the benefits of a simple structure and an easy procedure to design and fabricate.

REFERENCES

1. 5G PPP, "5G PPP architecture working group view on 5G architecture view on 5G architecture version 1.0, July 2016 5G PPP architecture working group view on 5G architecture," July 2016.
2. Wu, S. and B. Razavi, "A 900-MHz/1.8-GHz CMOS receiver for dual-band applications," *IEEE J. Solid-State Circuits*, Vol. 33, No. 12, 2178–2185, 1998.
3. Shi, L. and J. Gao, "Multitransmission zero dual-band bandpass filter using nonresonating node for 5G millimetre-wave application," *Act. Passiv. Electron. Components*, Vol. 2018, Article ID 7628598, 2018.

4. Xu, J., W. Wu, and C. Miao, "Compact microstrip dual-/tri-/quad-band bandpass filter using open stubs loaded shorted stepped-impedance resonator," *IEEE Trans. Microw. Theory Tech.*, Vol. 61, No. 9, 3187–3199, 2013, doi: 10.1109/TMTT.2013.2273759.
5. Cai, Q., Y. Li, X. Zhang, and W. Shen, "Wideband MIMO antenna array covering 3.3–7.1 GHz for 5G metal-rimmed smartphone applications," *IEEE Access*, Vol. 7, 142070–142084, 2019, doi: 10.1109/ACCESS.2019.2944681.
6. Holma, H. and A. Toskala, *5G Technology: 3GPP New Radio*, 2020.
7. Zhou, J., L. Wang, Z. Wang, S. Zhang, and M. He, "A compact quad-band bandpass filter with mixed electric and magnetic coupling," *Int. J. Microw. Wirel. Technol.*, Vol. 11, No. 5–6, 517–522, 2019, doi: 10.1017/S1759078719000357.
8. Liu, B., et al., "Quad-band BPF based on SLRs with inductive source and load coupling," *Electron. Lett.*, Vol. 53, No. 8, 540–542, 2017.
9. Zhang, Y., L. Gao, and X. Y. Zhang, "Compact quad-band bandpass filter for DCS/WLAN/WiMAX/5G Wi-Fi application," *IEEE Microw. Wirel. Components Lett.*, Vol. 25, No. 10, 645–647, 2015.
10. Wu, B., F. Qiu, and L. Lin, "Quad-band filter with high skirt selectivity using stub-loaded nested dual-open loop resonators," *Electron. Lett.*, Vol. 51, No. 2, 166–168, 2015.
11. Yan, T., X.-H. Tang, and J. Wang, "A novel quad-band bandpass filter using short stub loaded E-shaped resonators," *IEEE Microw. Wirel. Components Lett.*, Vol. 25, No. 8, 508–510, 2015.
12. Wu, H.-W. and C.-T. Chiu, "Design of compact multi-layered quad-band bandpass filter," *IEEE Microw. Wirel. Components Lett.*, Vol. 26, No. 11, 879–881, 2016.
13. Wei, F., Q. L. Huang, W. Li, and X. Shi, "A compact quad-band bandpass filter using novel stub-loaded SIR structure," *Microw. Opt. Technol. Lett.*, Vol. 56, No. 3, 538–542, 2014.
14. Cameron, R. J., C. M. Kudsia, and R. R. Mansour, *Microwave Filters for Communication Systems: Fundamentals, Design, and Applications*, John Wiley & Sons, 2018.
15. Wang, J., S. He, and D. Gan, "A 2.4/3.5/5.2/5.8-GHz quad-band BPF using SLRs and triangular loop resonators," *Electron. Lett.*, Vol. 54, No. 5, 299–301, 2018.
16. Sung, Y., "Simple quad-band bandpass filter implemented on a 50-Ω microstrip line," *Microw. Opt. Technol. Lett.*, Vol. 62, No. 1, 100–107, 2020, doi: 10.1002/mop.32016.
17. Xie, H., K. Zhou, C. Zhou, and W. Wu, "Analysis of four-stage stepped-impedance resonators and their application to quad-band microstrip bandpass filter," *Int. J. RF Microw. Comput. Eng.*, Vol. 30, No. 4, e22116, 2020.
18. Chen, C.-F., J.-J. Li, K.-W. Zhou, R.-Y. Chen, Z.-C. Wang, and Y.-H. He, "Design of a microstrip quad-band bandpass filter with controllable bandwidth and band spacing for multifunctional applications," *IET Microwaves, Antennas & Propagation* 374–380, 2020, doi: 10.1049/iet-map.2019.0563.
19. Cao, Q., H. Liu, and L. Gao, "Design of novel compact quad-band bandpass filter with high selectivity," *Frequenz*, Vol. 74, No. 1–2, 53–59, 2020, doi: 10.1515/freq-2019-0043.
20. Basit, A. and M. I. Khattak, "Designing modern compact microstrip planar quadband bandpass filter for hand held wireless applications," *Frequenz*, Vol. 74, No. 5–6, 219–227, 2020.
21. Wang, X., L. Wang, W. Yang, and Y. Zhang, "Design of quad-band filter using SIR and DGS," *2021 IEEE International Conference on Power Electronics, Computer Applications (ICPECA)*, 378–381, 2021.